

## Planar Spin Imaging by NMR

P. MANSFIELD AND A. A. MAUDSLEY

*Department of Physics, University of Nottingham,  
University Park, Nottingham NG7 2RD, U.K.*

Received July 30, 1977

A new method of spin-density imaging by NMR is described which allows simultaneous observation and differentiation of signals arising from spins distributed throughout a thin layer or plane within the specimen. The method, which is based on selective rf irradiation of the sample in switched magnetic field gradients, can produce visual pictures considerably faster than previously described line-scan imaging methods. Some simple examples of two-dimensional images obtained by the method are presented.

### 1. INTRODUCTION

During the last few years a number of methods have been described for producing nuclear magnetic resonance images related to the spin density distribution in solids and liquids (1-4). Of particular interest is the application of these imaging techniques in the study of biological material on a microscopic and a macroscopic scale.

Microscopic imaging at the cellular level offers a new method of studying localized relaxation times and diffusion processes within a single cell *in vitro*. Studies *in vivo* of water transport in plants is another interesting possibility.

At the macroscopic level, proton spin imaging *in vivo* could have clinical applications as a lower hazard alternative to X rays for medical imaging in man (5, 6). Known differences in the spin-lattice relaxation time between normal and malignant tissue (7, 8) might possibly be exploited for the early detection of cancer (6).

In all cases the important factors that comprise a general quality factor for the image are spatial resolution, signal/noise ratio, and the picture-formation time. Clearly, for a given imaging system, there is always some trade-off between signal/noise and picture-formation time. In an ideal system, all information from the spin distribution would arrive at a rate determined essentially by the experimenter and in this situation, the trade-off mentioned above would be straightforward. However, in practice it may not be possible to control the data input rate because of factors inherent in the imaging method itself. In addition, the information input may not be in a usable form, or it may take a considerable time to unravel the input or get it into a usable form. All the methods of imaging currently proposed attempt to reach the ideal, but they invariably fall short in one sense or another.

In this paper, which is an amplification and extension of our recent letter (9), we describe a new variant of the selective irradiation method of Garroway *et al.* (2), which allows simultaneous observation and differentiation of signals arising from spins distributed throughout a plane, or a set of planes within a three-dimensional object. By

this means, we show that the speed of image formation can be increased by an order of magnitude or so over that of the single line-scanning method of imaging recently demonstrated by Mansfield *et al.* (10). This speed is vitally important at both the microscopic and macroscopic extremes of specimen size if we are to see NMR imaging usefully applied to living systems. Experimental results demonstrating the imaging method together with some examples of planar images are also presented.

## 2. GENERAL DESCRIPTION OF METHOD

### 2.1. Selective Excitation in a Three-dimensional Object

Let the specimen be placed in a static magnetic field  $B_0$  which defines the  $y$  axis of quantization of the nuclei. We now describe three successive stages of selective irradiation and signal observation, (A), (B), and (C). This procedure closely follows that

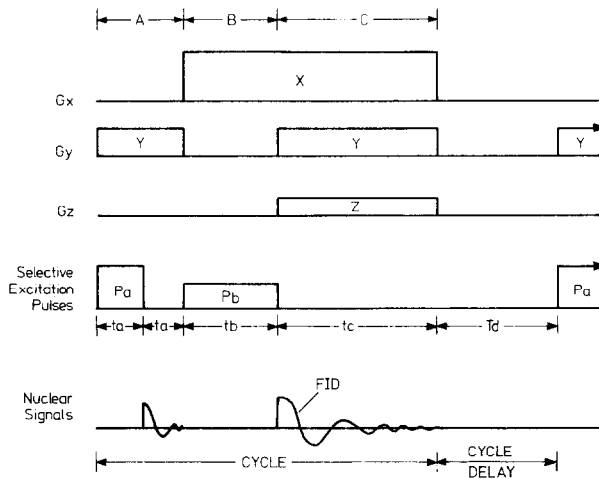


FIG. 1. Diagram of the switching sequence for three-dimensional spin imaging.

of Mansfield *et al.* (10). The order in which the various selections are performed is important in the practical realization of these imaging schemes. We describe a sequence which is less susceptible to pulse misalignments and relaxation effects. The particular order is indicated in Fig. 1, but other pulse permutations are also possible.

(A) In period A (Fig. 1), the gradient  $G_y$  is switched on and a selective irradiation pulse  $P_a$  is applied for time  $t_a$  in order to saturate regions of the specimen lying between a set of slices each of thickness  $\Delta y$  regularly spaced at  $y = y_0 + mb$  ( $m$  an integer) from the origin with grid separation  $b$  (Fig. 2). These slices comprise undisturbed layers (or planes) of magnetization in equilibrium with the static magnetic field  $B_0$ . After a further time  $t_a$ , the disturbed spins decay, producing an FID signal. If this signal is sampled and Fourier transformed, it yields the projection profile of the saturated regions of the sample and could be used for alignment purposes.

(B) We now concentrate on these slices of undisturbed spins (Fig. 2). In phase B,  $G_x$  alone is switched on and a second multiple-slit irradiation pattern  $P_b$  selectively excites the spins in a series of layers normal to the  $x$  axis for a time  $t_b$ . For a cylindrical sample as sketched in Fig. 3, these are a series of discs of thickness  $\Delta x$  spaced  $a$  apart. The

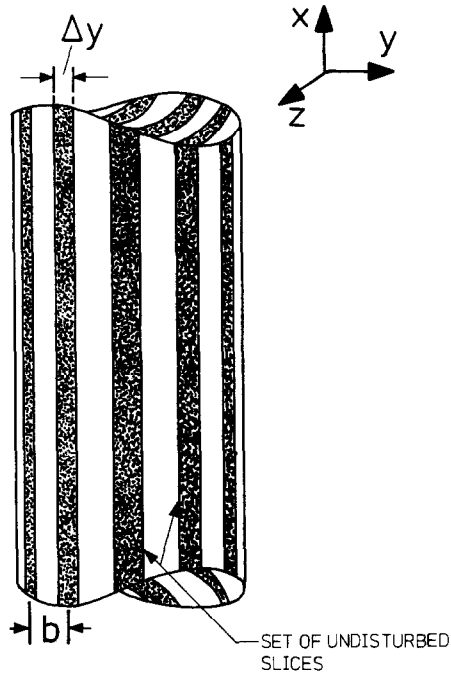


FIG. 2. Diagram showing the initially saturated regions in phase A together with the undisturbed slices in an extended cylindrical sample.

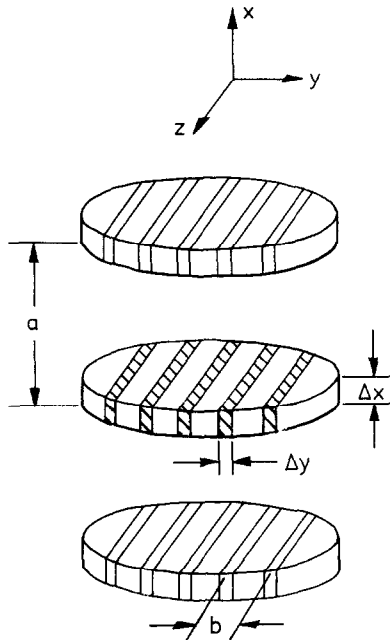


FIG. 3. Diagram showing the discs of magnetization selected in phase B. The active spin regions producing the FID signal are indicated by cross hatching.

shaded strips correspond to the active spin regions. The general undisturbed spin distribution is determined by the preparatory tailored pulse sequence, the details of which are discussed below.

The excitation pulses referred to here and previously could nutate the initially undisturbed spins through any angle  $\theta$ , but here we shall think of  $\theta$  as being  $90^\circ$ .

(C) At the end of the (B) excitation pulse, all three gradients are switched on so that the precessing spins experience the combined effects of  $G_x$ ,  $G_y$ , and  $G_z$ . (For imaging in a single plane, only  $G_y$  and  $G_z$  are required in the read period C.) The free induction decay (FID) from all volume elements  $mx\Delta y\Delta z$  spaced at  $y = y_0 + mb$  in the planes  $x = x_0 + la$  is observed and Fourier transformed to give a spin-density distribution within the solid  $\rho(x, y, z)$ .

In the simplest cyclic arrangement (Fig. 1), the spin system is left to recover in the cycle delay time  $T_d$  before repeating the sequence. In Section 4, however, we describe modifications to this procedure which enhance (or alternatively minimize) the effect on the FID of the various relaxation times.

## 2.2. Principle of Operation

The application of a magnetic field gradient to a three-dimensional or even a two-dimensional continuous distribution of spins will not ordinarily allow all elements of the distribution to be uniquely assigned magnetically. However, if they could be uniquely assigned then the "absorption" lineshape would in a single trace reveal the entire spin density distribution.

By a process of selective irradiation, a discrete lattice structure can be superimposed on the otherwise continuous spin distribution. That is to say, we can arrange that we observe only those spins lying on a well-defined lattice structure, the dimensions of which are controlled by selective excitation, etc.

For a given orthorhombic lattice, it is easy to convince oneself that all points can be uniquely assigned a definite frequency by application of *one* appropriately chosen gradient only. This process thus gives spot (point) checks, as it were, of the entire three-dimensional spin-density distribution. Spins between lattice points do not contribute to the observed signals. Enlargement of the points to include surrounding spins imposes constraints, as we shall see later, which may make it easier to look at a single plane, or a selected few planes, rather than the entire three-dimensional object. This may also be desirable from a data-handling and -storage point of view.

## 2.3 Theory

The initial selection and preparation of the spin system in period (A) involves the gradient  $G_y$  and rf pulses which nutate some of the spins through  $90^\circ$ . Precisely which spins are affected will depend on the magnitude of the field gradient and the spectral distribution of the perturbing tailored rf pulse.

For simplicity<sup>†</sup> we may represent the combined effects of such a tailored pulse and field gradient by a spatially selective operator  $(1 - \mathcal{S}_y)$ . If the spin-density distribution is  $\rho(xyz)$  then  $\mathcal{S}_y\rho(xyz)$  represents the undisturbed spin distribution while  $(1 - \mathcal{S}_y)\rho(xyz)$  is the distribution of spins which receives a  $90^\circ$  nutation pulse. In a similar manner, we introduce a second spatially selective operator  $\mathcal{S}_x$  which selects all the spins nutated

<sup>†</sup> Detailed calculations indicate that the effect of selective pulses on the spin system is somewhat more complicated than indicated here.

through  $90^\circ$  by the combined action of the second tailored excitation pulse and the new field gradient  $G_x$ .

In the following analysis, we assume ideal  $90^\circ$  nutations and no spin-lattice relaxation effects. In this case the operations referred to above are commutative.

Neglecting multiplicative constants, let the initial equilibrium density matrix of the spin system (spin  $I$ ) in the high-temperature approximation and distributed in volume  $v$  be

$$\sigma(0) = \int \delta_0 dv, \quad [1]$$

where  $\delta_0 = \rho(xyz)I_y$ . The  $z$  component of the transverse response signal in the rotating reference frame at time  $t$  is given by

$$S_z(t) = \text{Tr} \{ \sigma(t) I_z \}, \quad [2]$$

where  $\text{Tr}$  is the trace or diagonal sum.

After the first  $90^\circ$  pulse, the density operator describing the spin system at time  $t_a + t$  becomes

$$\delta_1(t_a + t) = \hat{S}_y \rho(xyz) I_y + (1 - \hat{S}_y) \rho(xyz) e^{i\gamma y G_y t} I_z e^{-i\gamma y G_y t}, \quad [3]$$

where  $\gamma$  is the magnetogyric ratio. The second term in Eq. [3] will give a transverse signal which quickly decays in  $t_a$ . Following the second  $90^\circ$  rf pulse, the density operator at time  $2t_a + t_b + t$  becomes

$$\begin{aligned} \delta_2(2t_a + t_b + t) = \hat{S}_x \exp(i\gamma t I_y [xG_x + yG_y + zG_z]) \tilde{\delta}_1(2t_a) \\ \times \exp(-i\gamma t I_y [xG_x + yG_y + zG_z]), \end{aligned} \quad [4]$$

where the tilde on  $\tilde{\delta}_1$  means that  $I_y$  is replaced by  $I_z$  and  $I_z$  by  $-I_y$  in  $\delta_1$ .

It is straightforward to show, by expanding Eq. [4] and substituting into Eq. [2], that the only significant nonvanishing signal following  $t_b$  at time  $t$  is

$$S(xyzt) = \int \hat{S}_y \hat{S}_x \rho(xyz) \cos \gamma t [xG_x + yG_y + zG_z] dv. \quad [5]$$

We have assumed, throughout, a noninteracting spin system which evolves during selective irradiation as though the rf pulse were a pure  $90^\circ$  rotation operator. No spin echo is expected following the second tailored  $90^\circ$  pulse since the field gradient change from  $\mathbf{j}G_y$  to  $\mathbf{G}$  will in general suppress it, except for those spins lying in a line along  $y$  corresponding to the magnetic centers of the gradients  $G_x$  and  $G_z$ , i.e., when  $x$  and  $z$  are both zero in Eq. [5]. These spins are likely to give a very small echo signal, which we entirely ignore in this analysis.

(a) *Fourier transform nesting.* In a generalization of these experiments we have in mind that the selection processes embodied in the operators  $\hat{S}_x$  and  $\hat{S}_y$  correspond not to single layers of material, but to multiple layers. We specialize to equally spaced layers of thickness  $\Delta x$ , strips of width  $\Delta y$ , and points of spacing  $\Delta z$  (set by sampling) with spatial periodicities  $a$ ,  $b$ ,  $c$ . In the limit where the undisturbed spin ranges  $\Delta x$ ,  $\Delta y$  approach zero, and for discrete sampling of the distribution along  $z$ , we have

$$\hat{S}_x \hat{S}_y \hat{S}_p \rho(xyz) \rightarrow \rho(la_1 mb_1 nc) = \rho_{lmn} \quad (l, m, n \text{ integers}), \quad [6]$$

where  $\hat{S}_z$  is the spatial sampling operator. The effective density, therefore, becomes a discrete distribution  $\rho_{lmn}$  corresponding to the lattice points  $x = al$ ,  $y = bm$ , and  $z = cn$ .

In this limit, the FID signal, Eq. [5], becomes

$$S = \sum \rho_{lmn} \cos t[l\Delta\omega_x + m\Delta\omega_y + n\Delta\omega_z]\Delta v_{lmn}, \quad [7]$$

where  $\Delta v_{lmn}$  is the volume of spins at a lattice point contributing to the signal, and is assumed to be constant for all points. The angular frequency increments are given by

$$\Delta\omega_x = \gamma a G_x, \quad \text{etc.} \quad [8]$$

We see from Eq. [7] that if the gradients and lattice constants are chosen so that

$$N\Delta\omega_z \leq \Delta\omega_y \leq \Delta\omega_x/M \quad [9]$$

where  $M$  and  $N$  are the largest values of  $m$  and  $n$ , respectively, all points in the distribution  $\rho_{lmn}$  are uniquely defined in the frequency domain. (Although we are talking here about superimposing a regular lattice by selective irradiation and sampling, the above point is true for a natural orthorhombic lattice.) A single Fourier transformation of  $S_{lmn}$  will thus yield in one calculation the complete three-dimensional distribution function  $\rho_{lmn}$ .

#### 2.4. Resolution

The requirement that all points in the object be simultaneously resolved is more stringent along the  $z$  axis. If there are  $N$  points spaced  $c$  apart, and each point has an extent  $\Delta z$ , then the condition for linearity of the  $z$  gradient is (11)

$$\Delta z/Nc = \Delta G/G_z, \quad [10]$$

where  $\Delta G$  is the deviation of  $G_z$  from uniformity. In addition, the natural linewidth of the resonance  $\Delta W_{\text{nat}}$  in the static field (which includes static field inhomogeneity, relaxation effects, diffusion in the gradient, and bulk broadening effects of the sample), must satisfy the relationship

$$\Delta W_{\text{nat}} \leq \Delta z G_z. \quad [11]$$

Of course, this stringency arises only if one wishes to put more information into a given bandwidth in the frequency domain. If the frequency per point along  $z$  is the same as in the line-scan experiment (10) then the requirements of both the  $z$  gradient coil and the natural linewidth, and hence the static field, are exactly the same.

On the other hand, if data are compressed into a narrow frequency band, they create higher demands on the uniformity of both the gradient coils and the static magnet. The advantage is a narrower bandwidth per picture point, giving an increased signal/noise ratio.

#### 2.5. Presentation and Readout of Data

The presentation and readout of data are perhaps best illustrated with a simple example of a three-dimensional image of a cylinder of mobile spins (water). We assume that the spin system has been selectively irradiated and prepared in phases (A) and (B) as described in Section 2.1 and we are about to observe the FID in phase (C).

Now the FID following the (B) phase selection can be read in  $G_x$  alone. In this case, all spins within a layer are undifferentiated, but of course the layers *are* differentiated so

the Fourier transform would simply be (for three layers, as in Fig. 3) three equal-amplitude spikes (Fig. 4a). However, if readout were done with  $G_x$  and  $G_y$  on, and in such a way that Eq. [9] is satisfied, namely, that  $\Delta\omega_x \geq M\Delta\omega_y$ , then we obtain the spectrum in Fig. 4b. The lineshape in this case consists of three equal spectra, each comprising the *discrete* projection profile for the cylinder. Finally, if the readout is performed in all three gradients  $G_x$ ,  $G_y$ , and  $G_z$  satisfying Eq. [9], we expect a discrete lineshape of constant amplitude, as indicated in Fig. 4c. Each element is ideally

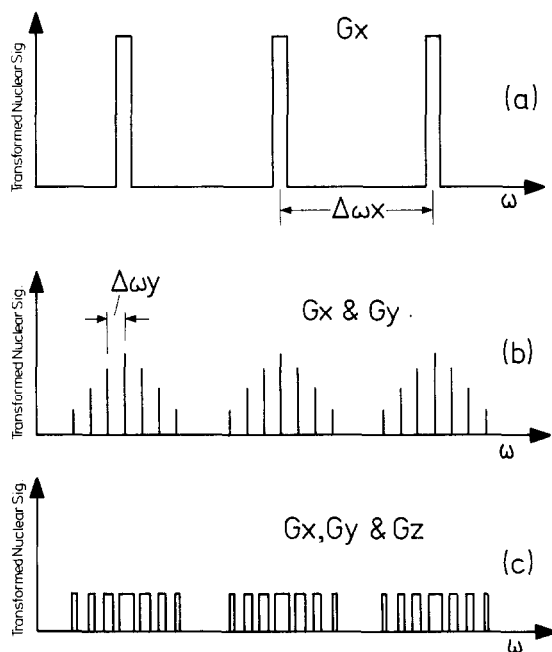


FIG. 4. Expected Fourier transformed signals for a cylindrical sample of homogeneously distributed spins prepared as in Fig. 3 by the selective irradiation procedure. (a) Signal with read gradient equal to  $G_x$  only, showing three equal lines corresponding to the signals from the three discs of magnetization as in Fig. 3. (b) Each of the three lines in (a) is split by the addition of  $G_y$ . The discrete profile corresponds to the projection of the spin-density distribution of the disc along the  $y$  axis. (c) Expected signal on application of all three gradients, as in an imaging experiment. The addition of  $G_z$  broadens each line of the discrete spectrum in (b) above. Ideally, the profile of each broadened line is rectangular and of constant height, giving a direct visual picture of successive cross-sectional views through the discs.

rectangular, with the width varying across the spectrum as indicated, and represents a cross-sectional profile of each strip within the layer.

### 2.6. Tailored rf Pulses

Unlike line-scan imaging (10) the tailored rf pulse sequences in these experiments have a multiple discrete spectral distribution as illustrated in Fig. 5 for the special cases of (a) rectangular spectral profiles, and (b) uniform amplitude. That is to say, instead of scanning line by line, the entire object is irradiated at the same time. (In certain cases, it is possible to compensate for rf inhomogeneity in the transmitter coil system by changing the spectral profile from a constant amplitude to something which varies with frequency in the desired manner.)

For a multiple discrete rf spectral distribution of  $L$  components with constant amplitude  $H_{1\omega}$ , individual constant widths  $m\Delta\omega_p$  ( $m$  an integer) and with the center frequency of each component separated by  $\Delta\omega_l = n\Delta\omega_p$ , the time domain pulse must be shaped according to the expression

$$H_1(t_n) = H_{1\omega} m \Delta\omega_p \operatorname{sinc}(\Delta\omega_p m t_n) \sum_0^L e^{i(l\Delta\omega_p t_n)}. \quad [12]$$

In this expression, the angular frequency per point is given by

$$\Delta\omega_p = 2\pi/N\tau, \quad [13]$$

in which  $N$  is the total number of points in the time domain and  $\tau$  is their spacing.

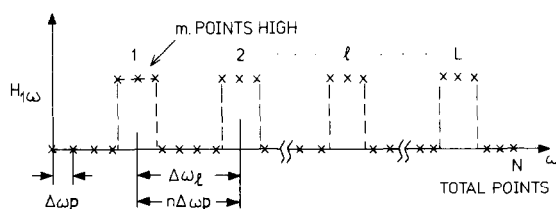


FIG. 5. Diagram of the discrete multiple rectangular spectral distribution for the tailored rf pulse applied in  $t_n$ .

Of course, if an additional frequency offset is added so that image fields are nonsecular as far as the resonant spins are concerned (i.e., outside the range of frequencies produced by the field gradient), then we take the real part of the expression and simply compute the cosine transform.

Equation [12] gives the initial rf pulse amplitude

$$H_1(0) = 2\pi L m H_{1\omega} / N\tau, \quad [14]$$

where  $H_1(0)/Lm$  is the field amplitude used to calculate the  $90^\circ$  pulse condition for each irradiated point.

(a) *Pulse sequence.* The A irradiation pattern could look like Fig. 5 with  $m$  large and  $m - n$  small, corresponding to narrow gaps of zero  $H_{1\omega}$  intensity, which in turn correspond to the unirradiated and hence undisturbed magnetization in Fig. 2. However, it is technically more convenient because of rf power requirements to produce a complementary radiation pattern corresponding to small  $m$ , but this does just the opposite of what is required. That is to say, it disturbs the narrow strips that we wish to leave undisturbed.

One procedure, therefore, is to pulse with rf having a spectral distribution pattern which is complementary to that required. This is followed immediately with a short  $90^\circ$  rf pulse whose rf carrier phase is shifted by  $180^\circ$ . The net effect is thus to tip the magnetization in the narrow strips back up along the  $y$  axis, while the undisturbed magnetization in the wider strips is tipped backward by  $90^\circ$  into the  $x$ - $z$  plane of the rotating reference frame.

The pulse shaping referred to is achieved in our case by computing on-line the Fourier transform of the desired rf spectral distribution, which is then used to modulate directly the rf pulse envelope (10).

It is also possible to approximate the complementary rf spectral distribution by a train of equally spaced short rf pulses. The discrete frequency distribution of such a pulse train has a width inversely proportional to pulse duration, a periodicity inversely proportional to the pulse repetition period, and a discrete linewidth inversely proportional to the pulse train length. The spectral distribution may be reasonably approximated as constant over a restricted frequency range. However, generating a pulse spectrum wider than required, in order to satisfy the constant-amplitude approximation, represents a considerable waste of rf power in the unwanted sidebands and is best avoided, particularly when irradiating live specimens.

2.7. *Effects of Finite Selection Width*

The condition for magnetic uniqueness, expression [9], was derived for point regions of spins within a general three-dimensional object and it ignored the effect of finite volume of the sample at the lattice sites.

If the elemental volume at all lattice sites is  $dv = \Delta x \Delta y \Delta z$ , then additional constraints on the size of this volume and the magnitude of the gradients arise if all points are to be simultaneously resolved. In this case the inequality, expression [9], is modified and becomes

$$\delta\omega_x + \delta\omega_y + N\Delta\omega_z \leq \Delta\omega_y \leq (1/M)[\Delta\omega_x - \delta\omega_x - \delta\omega_y], \quad [15]$$

where  $\delta\omega_x = \Delta x G_x$  and  $\delta\omega_y = \Delta y G_y$ .

The advantage of expanding the elemental volume is of course that more of the sample contributes to the observed signal. However, as we shall see, the price paid for this increase in sensitivity is the measurement of an average spin density over the volume, or in other words a decrease in spatial resolution.

We now enquire in detail into the effect of the additional contributions to the FID signal when the discrete lines of the rf spectral distribution, during selection, have a finite width. For simplicity we consider the case of single-plane imaging. That is to say, the FID is read in the two gradients  $G_y$  and  $G_z$  only. However, the arguments developed will be applicable to more general multiplanar imaging.

Suppose now that we do not have delta functions, but a set  $M$  of broad spikes or even rectangular spectral distributions (Fig. 5) which in one gradient  $G_y$  produce the discrete density projection profile  $f_m(\omega_{mq})$  along the  $y$  axis. The  $m$ th spike or rectangle can be regarded as being made up of a closely spaced set  $q$  of delta functions, each one of which would broaden in combined gradients  $G_y$  and  $G_z$  to yield the  $z$ -axis density function  $\rho_z^{mq}(\omega_{mq})$ . Thus over the subset  $q$  the observed profile will be a broadened, smeared function  $\Gamma_m(\omega_{mq})$  which is the weighted sum of individual functions, i.e., the convolution-like function

$$\Gamma_m(\omega_{mq}) = \sum_q \rho_z^{q'm}(\omega_{q'm}) f_m(\omega_{mq'} - \omega_{mq}). \quad [16]$$

We note that, unlike the ordinary convolution function, the broadening function  $f_m(\omega_{mq})$  varies in general with  $m$  across the projection.

For a closely spaced subset, Eq. [16] reduces to

$$\Gamma_m(\omega) \rightarrow \int \rho_z^m(\omega') f_m(\omega' - \omega) d\omega', \quad [17]$$

where the discrete variables  $\omega_{mq}$  and  $\omega_{mq'}$  are replaced by the continuous variables  $\omega$  and  $\omega'$ .

For a set of well-resolved spikes (or ideally, delta functions) where the extent of the additional broadening produced by  $G_x$  does not overlap, we get from Eq. [17]

$$\Gamma_m(\omega) = \rho_z^m(\omega). \quad [18]$$

This is the result already obtained and illustrated (Fig. 6). But Eq. [16] also allows the evaluation of  $\rho_z^{mq}(\omega_{mq})$  when  $f(\omega)$  is not a delta function, provided the  $m$ th cross-sectional profile does not change significantly with  $q$ , i.e., if we replace  $\rho_z^{mq}(\omega_{mq})$  by  $\rho_z^m(\omega_{mq})$ , which corresponds to a high degree of short-range spatial correlation. In this case Eq. [17] is a localized convolution integral. The function  $\rho_z^m(\omega_{mq})$  can be obtained

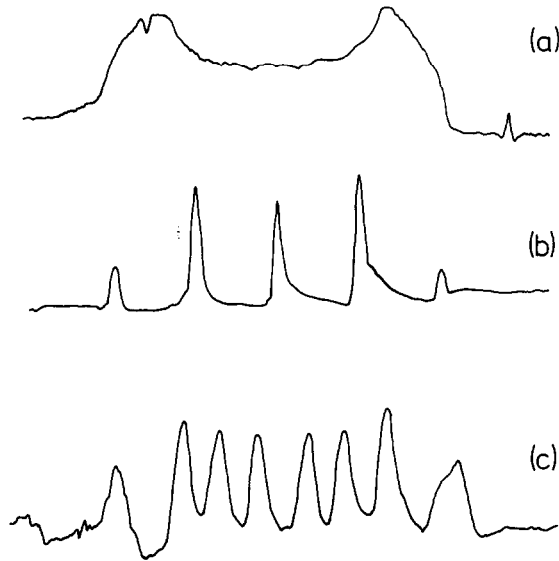


FIG. 6. Experimental results obtained from a mineral oil annulus. (a) Projection of the annulus in a static field gradient  $G_y = 0.95 \text{ G cm}^{-1}$ . The signal was averaged 39 times. (b) response profile when the annulus is irradiated with a discrete spectral distribution in  $G_y$  only (see text). (c) Response profile of annulus to discrete spectral irradiation as in (b) above, but with additional read gradient  $G_z = 0.266 \text{ G cm}^{-1}$  switched on. The signals in (b) and (c) were averaged 128 times.

directly from the Fourier transform of  $\Gamma_m(\omega_{mq})$  and the localized projection profile  $f_m(\omega_{mq})$  without the additional broadening of  $G_x$ .

The procedure for single-plane images, for example, is thus first to measure the discrete projection profile in  $G_y$  alone. Next the broadened profile is recorded in both gradients  $G_y$  and  $G_z$ . Each discrete section of both profiles is inversely Fourier transformed to the time domain and the broadened signal is divided by the corresponding unbroadened signal computed at zero frequency offset. The quotient is then Fourier transformed back to the frequency domain, and the resulting signal represents the true density profile along the  $z$  axis.

### 3. EXPERIMENTAL RESULTS

The results described here were obtained at 15.0 MHz with a computer-controlled spectrometer which has been substantially described elsewhere (10). In the present

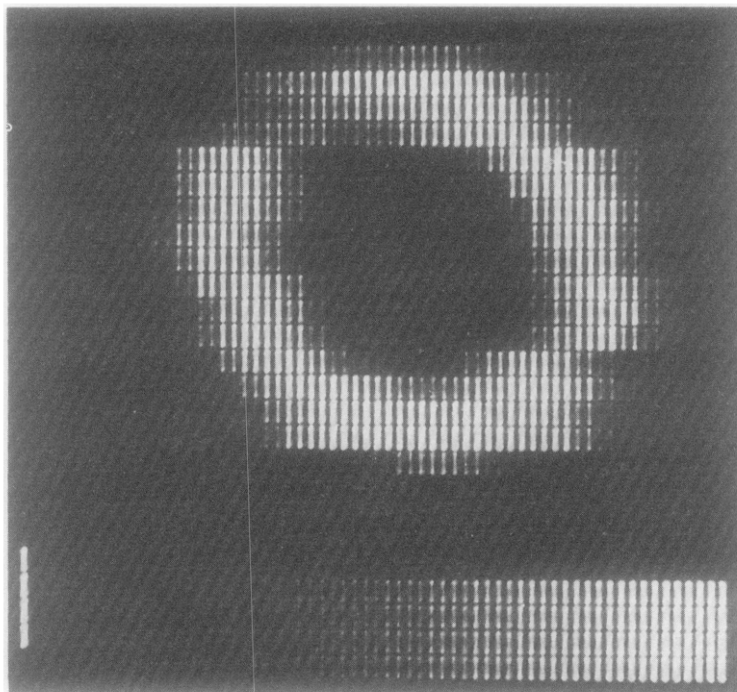


FIG. 7. A cross-sectional proton spin-density image of a mineral oil annulus produced by planar spin imaging using the data of Fig. 6c. An intensity scale corresponding to a 16-level linear density wedge is also included across the bottom of the picture.

experiments, however, an orthogonal transmitter and receiver coil system was used (6, 12). The planar imaging method has been tried out for protons in a liquid mineral oil sample in the form of a cylindrical annulus. The measured outer and inner diameters of the annulus were 13.7 and 8.1 mm, respectively. For simplicity, specialization to a

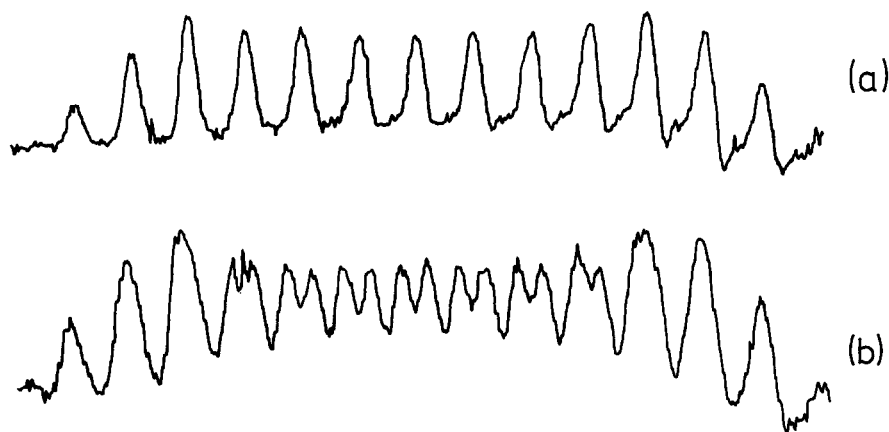


FIG. 8. (a) Discrete projection spectrum of a mineral oil annulus comprising 13 lines. This was obtained by irradiating and reading in  $G_y$  only. (b) Response profile as in (a) above, but broadened in the read phase by additional gradient  $G_z$ . (See text for details.)

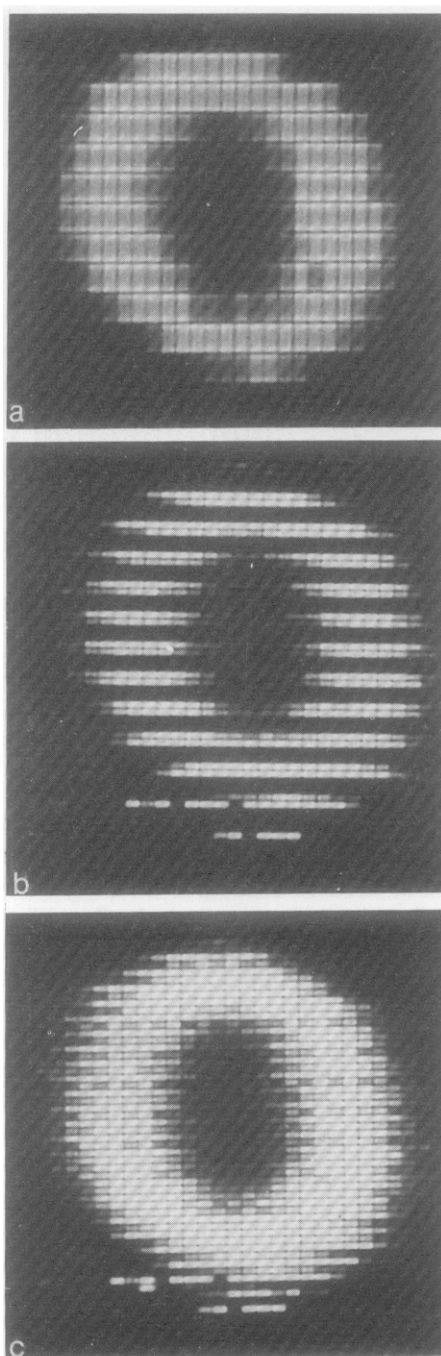


FIG. 9. Planar spin images from protons in a mineral oil annulus showing buildup of the image with a fourfold interlace. (a) Coarse planar image obtained with data similar to those of Fig. 8b. Spot wobbling has been used to fill in the gaps between individual spots. (b) Second stage of the fourfold interlace pictures. The spot size is reduced to avoid overlap. (c) Complete fourfold interlace image. See text for details.

layer of material by selective irradiation is not employed since the sample has cylindrical symmetry along the  $x$  axis. The cycle thus starts in phase B (Fig. 1) with  $G_z$  switched off and  $G_y$  switched on throughout.

The one-dimensional projection of the annulus measured in  $G_y$  is shown in Fig. 6a. The sample was selectively irradiated with a tailored pulse corresponding to five equally spaced, equal-intensity rectangular peaks in the rf spectral distribution arranged to just span the sample. That is to say,  $L = 5$ ,  $m = 1$ , and  $n = 20$  (see Fig. 5). The frequency per point,  $\Delta\omega_p$ , is  $855 \text{ rad sec}^{-1}$ . The response to this selective irradiation in the gradient  $G_y$  is shown in Fig. 6b. As expected, it is the discrete projection profile. If more lines were included, we would end up tracing out the continuous projection profile (Fig. 6a). The width of each spike in Fig. 6b is 195 Hz. About half the broadening of these spikes is due to static magnetic field inhomogeneity, the remainder being ascribed to nonlinearity of the field gradient coils.

The response to the selective irradiation in  $G_y$  read in  $G_y$  and  $G_z$  is shown in Fig. 6c. Each spike of Fig. 6b is broadened by the action of the additional field gradient  $G_z$  to yield directly the planar spin distribution in the form of successive cross-sectional views through the oil annulus. The distribution has a fairly coarse grid along the  $y$  direction. A finer grid was obtained by an interlacing procedure in which the radiation pattern was shifted up in frequency by one-fourth, one-half, and three-fourths of the frequency spacing between adjacent peaks in the rf spectral distribution. This gives a fourfold finer grid resolution across the specimen and has thus allowed us to produce a visual image. This is shown in Fig. 7 and consists of a  $20 \times 40$  array made up from four spectra, as in Fig. 6c. Each broadened spectrum is the result of 128 averages. The transformed data are used to modulate the spot intensity of an oscilloscope in a television raster display (13). A linear grey scale of 16 levels of spot brightness covering the range black to white is used. The picture resolution in Fig. 7 was limited by a maximum of 256 Fourier-transformed points in the frequency domain. Increasing this number to 512 (1024 in the time domain) has improved both the resolution and the speed with which a planar image can be produced. Fig. 8a shows another discrete one-dimensional projection of the annulus in  $G_y$ . In this case the discrete excitation spectrum had 16 equal-intensity peaks, that is to say  $L = 16$ ,  $m = 1$ , and  $n = 8$  (see Fig. 5). The response to this excitation spectrum applied in  $G_y$  and read in combined gradients  $G_y$  and  $G_z$  is shown in Fig. 8b and is an average of 16 spectra. The gradient values,  $G_y = 1.86 \text{ G cm}^{-1}$  and  $G_z = 0.1 \text{ G cm}^{-1}$ , were arranged so that the excitation spectrum spanned the annulus with some overlap.

The planar image corresponding to Fig. 8b is shown in Fig. 9a and has a resolution of 16 elements along the vertical picture axis. The horizontal picture axis has a total of 32 elements. With a cycle delay of 0.3 sec, this picture took 7.8 sec to produce, which includes 3.0 sec for the 1024-point time domain Fourier transform. Figure 9b shows the second stage of a fourfold interlace, and Fig. 9c the complete fourfold interlace planar image. The whole picture took 37.2 sec to produce and is a  $64 \times 32$  array. This is 16 times faster than producing an equivalent picture by single line scanning (10). The broadening of the spikes in Fig. 8a is due to static field inhomogeneity and nonlinearity of the  $y$  axis gradient and we suspect that it is the principal cause of degradation of the spectrum in Fig. 8b. Preliminary tests of the localized deconvolution procedure outlined in Section 2.7 show that the method will remove broadening due to the static field

inhomogeneity and gradient coils as well as broadening due to finite width of the rf irradiation pattern. However, full picture enhancement on-line has not so far been tried out because of computer core limitations.

#### 4. IMAGING CYCLE VARIANTS

##### 4.1. $T_1$ Discrimination

The basic planar imaging method described in Section 2 and Fig. 1 is  $T_1$  selective through the cycle delay  $T_d$  and can thus discriminate against regions of the specimen having a spin-lattice relaxation time longer than  $T_d$ . However, from the point of view of data accumulation, this delay represents wasted time, and hence a low efficiency in information input, since the FID is zero in this period.

##### 4.2. $T_2$ and $T_1$ Discrimination

The transverse signal can be made to persist following the initial FID by recalling the signal in a series of spin echoes. This may be done with  $T_d$  zero or short by either (i) periodically reversing all gradients in an extended C phase, or (ii) applying a train of  $180^\circ$  rf pulses in a Carr-Purcell sequence, again in an extended C phase with static gradients. Method (i) is unlikely to give additional echoes from the initially saturated spins in (A) and will work perfectly for single-plane imaging when  $G_x = 0$  in the read phase (C). Method (ii) will work satisfactorily for single-plane imaging, but for multiplanar imaging the  $180^\circ$  pulses will affect the initially saturated spins in (A). However, this is unlikely to produce an extra echo for the same reason as that in case (i) above, namely, that the additional gradients  $G_y$  and  $G_z$  will tend to quench the formation of any echo. The timing of the pulse sequence also does not favor the formation of an observable signal.

The peak echo amplitude decays with time constant  $T_2$ . Thus if  $T_2 \gg t_b$ , many field gradient reversals can be made and many echoes can be produced. These echoes can be suitably co-added to improve the signal/noise ratio over that of the single FID signal.

The echo-averaging process described here allows the transverse decay signal, in effect, to persist for a time  $T_2$  or so. If  $T_1 \simeq T_2$  there is no wait period required between the end of signal averaging and the repeat of the A phase in the following cycle. In biological materials, however,  $T_2$  can be less than  $T_1$  and in this case time could be wasted waiting for the spin system to repolarize. Nevertheless this method could find useful application since for  $T_2 < T_1$ , it will produce images which discriminate against regions of the specimen with short  $T_2$ . For  $T_2 \simeq T_1$  the method discriminates against regions of short  $T_1$  and thus acts in a manner complementary to that of the basic method described in A above.

##### 4.3. Relaxation-Time-independent Methods

Relaxation time discrimination can be of considerable value in enhancing picture contrast in medical images (6). However, for images representing true spin-density variations, relaxation time discrimination can be a problem. We now introduce modifications to the cycle of Fig. 1 which substantially remove relaxation time dependences and improve the data-sampling efficiency.

The modified cycle is shown in Fig. 10 and should run continuously. The A and B phases are the same as indicated in Fig. 1. The read phase C is similar to that described previously, and although one FID and one-half spin echo are shown, this phase could be extended from  $2t_c$  to  $2nt_c$  (where  $n$  is an integer) to include more echoes.

The new feature of the cycle is the store phase D. As indicated, the refocused signal at a spin-echo peak is switched back to the equilibrium position by the same selective excitation pulse  $P_b$  but with a  $180^\circ$  rf carrier phase shift denoted  $P_b^{180}$ . Any magnetization loss in the read and store periods can be recovered in the delay period. Of

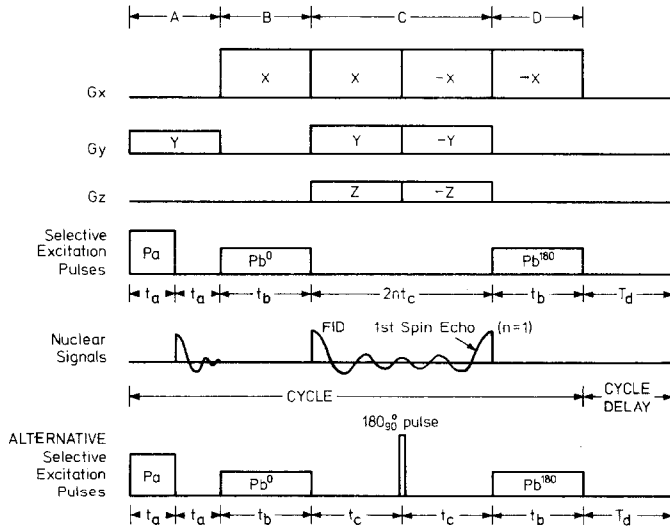


FIG. 10. Diagram of a modified switching sequence for multilayer three-dimensional spin imaging. The main object of this modification is to enable rapid cycling of the sequence in times less than  $T_1$  and  $T_2$ . An alternative arrangement of the selective excitation pulses is also shown. In this case, the field gradient reversals are not required.

course, the recovery of magnetization may not exactly balance any losses, so that the initial FID signal amplitude may, after a number of cycles, approach a new equilibrium magnetization, different from the static equilibrium value, whose amplitude is optimized by varying the cycle delay  $T_d$ . The important point is that the read signal is substantially independent of both  $T_1$  and  $T_2$  for  $2nt_c \ll T_2, T_1$ .

In a given cycle, the fraction of time spent reading the signal can be increased by including more echoes. The maximum time  $2nt_c$  is, of course, limited to  $T_2$  but it will probably be better to keep  $n$  of the order of 1 or 2 because of the relaxational losses in the signal amplitude.

A number of alternative and equivalent excitation pulse arrangements are also shown which use  $180^\circ$  rf pulses to refocus the spin echo. (The gradient reversals are *not* required in this case.) Notice that the  $180^\circ$  carrier phase shift of the second selective pulse  $P_b$  is still required. The disadvantage of this arrangement is that more rf power is required, but this could be outweighed in a practical system by the greater simplicity achieved.

Using rf pulses to refocus (without gradient reversals) for the read phase is similar to the driven equilibrium Fourier transform (DEFT) method of signal enhancement described by Becker *et al.* (14). A number of modifications to this method proposed by Waugh (15) are also incorporated in our Fig. 10. These modifications are to the carrier phasing of the  $180^\circ$  refocusing pulses, with respect to the  $P_b$  selective excitation pulse. Thus strictly speaking, the  $180_{90}^\circ$  rf pulses referred to in Fig. 10 should really be selective excitation pulses as well, with the same sharp spectral profile as  $P_b^0$  and  $P_b^{180}$ . The object of introducing these apparent complications in the rf carrier phasing is to compensate the cycle automatically for imperfections due to rf inhomogeneity. If parts of the specimen do not receive an exact  $180^\circ$  rf pulse, then repeated applications of the cycle will in general lead to a deterioration and perhaps complete loss of the signal. For proper compensation, it is better to have  $n = 2$ , thus producing two spin echoes between  $P_b^0$  and  $P_b^{180}$ . In the rf pulse version, refocusing can be achieved by using either  $180_{90}^\circ$  rf pulses for all  $n$  or  $180_0^\circ$  ( $n$  odd) and  $180_{180}^\circ$  ( $n$  even) pulses. Alternate phase reversal in this alternative  $180^\circ$  pulse arrangement produces alternate sign reversals of the spin echoes. Co-addition of these for signal averaging should therefore take account of the sign changes.

(a) *A simpler cycle.* Under the right conditions, repetitive selective excitation pulses  $P_b$ , as in the simple imaging method of Fig. 1, can be made to produce a nonzero FID in a quasi-equilibrium state, even when the cycle delay  $T_d$  is a lot less than the spin-lattice relaxation time  $T_1$ . This effect has been described by Carr (16) and others (4, 17, 18) and is often referred to as steady-state free precession (SSFP). We have observed experimentally that SSFP works for selective irradiation pulses and in switched magnetic field gradients.

As in the previous modified cycle above, an advantage of combining our new imaging method with SSFP is that the image produced is substantially independent of both  $T_1$  and  $T_2$ .

## 5. PICTURE QUALITY AND PERFORMANCE

A useful measure of the performance of a particular imaging scheme is the imaging time  $T_i$  (10). This is defined as the total time required to produce a picture to a given resolution and signal/noise ratio. The imaging time clearly depends on the imaging method, and indeed, even for the same method, can vary depending on precisely how the data obtained are processed.

For a given three-dimensional spin system, there is a limited amount of information which has to be read out, processed, and displayed. Quite irrespective of the imaging method used to access this information, there are a number of fundamental constraints which allow an ideal imaging time to be calculated.

### 5.1. Imaging Time

Let us divide the imaging volume field, assumed to be a cube, into  $m^3$  volume elements. For each volume element there is a corresponding picture element in the image field and we assume that only the spins in a fraction  $\beta$  of each volume element contribute to the observed signal for each picture point. The signal/noise ratio per picture point,  $R_p$ , is given by (10)

$$R_p = Af(Q\omega_0^3\beta V/B)^{1/2} = R_{p_0}/\beta^{1/2} \quad [19]$$

where  $V$  is the total volume of the sample assumed to fill the resonant receiver coil completely with a distribution of mobile spins, and  $f = 1/m^3$  is the filling factor for one picture volume element. The quantities  $Q$ ,  $\omega_0$ , and  $B$  are, respectively, the receiver coil quality factor, the Larmor angular frequency of the spins, and the bandwidth per picture point. The constant  $A$  embodies the spin susceptibility, the receiver temperature and noise figure, and a coil geometry factor. We now assume that data from all  $m^3$  volume elements can be collected simultaneously, but in such a way as to preserve the spatial localization of each element. That is to say, we consider a planar or multiplanar imaging system such as that described in Fig. 10, for example.

The imaging time  $T_i$  is given quite generally by

$$T_i = N_A T_c + D_{lmn}, \quad [20]$$

where  $N_A$  is the number of averages of the imaging cycle necessary to achieve the desired signal/noise ratio  $R$ , and  $D_{lmn}$  is the time required to Fourier transform the data into  $l \times m \times n$  picture points. The cycle period  $T_c$  (see Fig. 10) is given by

$$T_c = 2t_a + 2t_b + 2nt_c + T_d, \quad [21]$$

in which  $2nt_c$  is the data collection time,  $t_a$  and  $t_b$  are selective excitation pulse lengths, and  $T_d$  is a delay which incorporates the time to compute the Fourier transforms of the selective irradiation excitation spectra. The bandwidth per point  $B$  of Eq. [19] can be expressed in terms of a single data-collection interval as

$$B = 2\pi/t_c. \quad [22]$$

The signal/noise ratio enhancement produced by averaging the signal  $2nN_A$  times is given by

$$R = R_p (2nN_A)^{1/2}. \quad [23]$$

From Eqs. [19] and [20] it is clear theoretically that the shortest imaging time  $T_{i\min}$  is achieved when the signal from all the spins in the specimen is sampled all of the time. i.e., when  $\beta = 1$  and  $T_c = 2nt_c$ . Practical imaging systems, which inevitably fall short of this ideal, can, however, be simply compared with it by introducing an imaging efficiency  $\eta_i$  defined by

$$\eta_i = T_{i\min}/T_i, \quad [24]$$

which, from Eqs. [19], [20], and [21], reduces to

$$\eta_i = \alpha\beta, \quad [25]$$

where  $\alpha = 2nt_c/T_c$ . The Fourier transformation time, which depends on the type of computing facility available, has been ignored in this calculation.

In the selective irradiation scheme for planar imaging, some space must be allowed between adjacent line elements. This means that  $\beta$  cannot be unity unless interlacing of the picture is used. This is discussed in Section 5.2. The nature of the selective pulses also means that  $\alpha$  cannot equal unity. Realistic values of  $\alpha$  and  $\beta$  for single-plane imaging as described in this paper would be  $\alpha = \frac{1}{2}$  and  $\beta = \frac{1}{4}$ , yielding an efficiency  $\eta_i = 12\%$ .

### 5.2. Comparison with Line Scanning

It is of interest to compare the imaging times for single-plane and line-scan imaging under optimum conditions for equal signal/noise ratio and resolution. If we consider pictures comprising equally spaced grids of  $m$  lines in both cases, then the necessary gaps between adjacent lines in planar imaging mean in general that  $\beta^l$  can be greater than  $\beta^p$ , where the superscripts  $l$  and  $p$  used here and later refer, respectively, to line scan and planar imaging.

An alternative way of leaving unfilled gaps in the planar image is the idea of interlacing, already discussed and used to produce the NMR images presented in Section 3. In this case it is straightforward to arrange that  $\beta^l = \beta^p$ , corresponding to the final fine grid required for a given picture resolution. However, the final planar image is then made up of an interlace of  $i$  (*integer*) coarser grid planar images produced by selective irradiation with  $m/i$  lines. The necessary gap between adjacent rows in each coarse planar image is thus created by the missing  $(i - 1)$  lines. In this case and from Eqs. [19], [20], and [23] we obtain for the single-plane imaging of  $m^2$  points in an  $i$ -fold interlace

$$T_i^p = (i/2n) \left( \frac{R}{R_{p_0}} \right)^2 \frac{T_c^p}{\beta^p} + iD_{m^2/i}^p \quad [26]$$

Line scanning the same data in  $m$  rows with  $m$  points per row yields an imaging time (using the same receiver and bandwidth per point)

$$T_i^l = (m/2n) \left( \frac{R}{R_{p_0}} \right)^2 \frac{T_c^l}{\beta^l} + mD_m^l \quad [27]$$

If we take  $T_c^p = T_c^l$ ,  $\beta^p = \beta^l$  and discard the Fourier transformation times then the imaging time ratio is

$$T_i^l/T_i^p = m/i. \quad [28]$$

Of course, account of the Fourier transformation times may be made by using the exact expressions [26] and [27]. Using fast computers, Fourier transformation of data into an array of  $128 \times 128$  data points can be performed in about 3.5 sec. When the first term in Eq. [26] is comparable to  $iD_{m^2/i}^p$ , then if  $iD_{m^2/i}^p \simeq md_m^l$ , the imaging time ratio becomes for large  $m$

$$T_i^l/T_i^p \simeq m/2i, \quad [29]$$

which still represents a substantial improvement in speed for planar imaging over line scanning. Taking  $m = 128$  and a fourfold interlace, Eq. [29] shows that in a typical situation planar imaging is 16 times faster than line scanning. Line scanning under these conditions yields an imaging efficiency  $\eta_i$  of only 0.24%.

## 6. DISCUSSION AND CONCLUSIONS

We have shown both experimentally and theoretically that, by a process of selective irradiation in switched magnetic field gradients, it is possible to receive and differentiate NMR signals arising simultaneously from spins distributed throughout a thin slice or

plane within a specimen. These signals can be used to produce a visual image related to the spin-density distribution throughout the slice. Initial applications of planar imaging are likely to be limited to forming pictures one plane at a time. However, our analysis shows that it is possible to produce simultaneous multiplanar images.

For the most efficient generalized imaging system one would ideally wish to observe all the spins distributed within the specimen all of the time. In the planar image of Fig. 9a only one-fourth of the total number of spins in the slice contributed to the signal. With improved gradient coils and by using localized deconvolution, it should be possible to increase this fraction, to between one-half and one-third. Ways of increasing the data acquisition time are also proposed. Using a version of the DEFT technique (14, 15) in conjunction with planar imaging, one could increase the fraction of total time available for data acquisition to between one-fourth and one-half. A similar improvement might be obtained by using planar imaging in combination with SSFP (17, 18). Both methods should produce planar images which are substantially independent of relaxation time effects.

The fact that signals arise from selected regions throughout a plane or slice means that planar spin imaging is in principle faster than the single line-scanning method for the same signal/noise ratio and resolution. As an example, we can produce a one-shot planar image comprising a  $16 \times 32$  data array in 30 msec plus the Fourier transformation time, with a signal/noise ratio of the image of about 4:1. Under optimum line-scanning conditions the same image would take 16 times longer to produce.

#### ACKNOWLEDGMENT

We are grateful to the Science Research Council for an equipment grant.

#### REFERENCES

1. P. C. LAUTERBUR, *Pure Appl. Chem.* **40**, 149 (1974).
2. A. N. GARROWAY, P. K. GRANNELL, AND P. MANSFIELD, *J. Phys. C* **7**, L457 (1974).
3. A. KUMAR, D. WELTI, AND R. R. ERNST, *J. Magn. Resonance* **18**, 69 (1975).
4. W. S. HINSHAW, *J. Appl. Phys.* **47**, 3709 (1976).
5. P. MANSFIELD AND A. A. MAUDSLEY, *Phys. Med. Biol.* **21**, 846 (1976).
6. P. MANSFIELD AND A. A. MAUDSLEY, *Brit. J. Radiol.* **50**, 188 (1977).
7. R. DAMADIAN, *Science* **171**, 1151 (1971).
8. J. G. DIEGEL AND M. M. PINTAR, *J. Nat. Cancer Inst.* **55**, 725 (1975).
9. P. MANSFIELD AND A. A. MAUDSLEY, *J. Phys. C* **9**, L409 (1976).
10. P. MANSFIELD, A. A. MAUDSLEY, AND T. BAINES, *J. Phys. E* **9**, 271 (1976).
11. P. MANSFIELD AND P. K. GRANNELL, *Phys. Rev.* **12**, 3618 (1975).
12. D. M. GINSBERG AND M. J. MELCHNER, *Rev. Sci. Instrum.* **41**, 122 (1970).
13. T. BAINES AND P. MANSFIELD, *J. Phys. E* **9**, 809 (1975).
14. E. D. BECKER, J. A. FERRETTI, AND J. C. FARRAR, *J. Amer. Chem. Soc.* **91**, 7784 (1969).
15. J. S. WAUGH, *J. Mol. Spectrosc.* **35**, 298 (1970).
16. H. Y. CARR, *Phys. Rev.* **112**, 1693 (1958).
17. R. R. ERNST AND W. A. ANDERSON, *Rev. Sci. Instrum.* **37**, 93 (1966).
18. R. FREEMAN AND H. D. W. HILL, *J. Magn. Resonance* **4**, 366 (1971).